

# Crystallize It before It Diffuses: Kinetic Stabilization of Thin-Film Phosphorus-Rich Semiconductor CuP<sub>2</sub>

Andrea Crovetto,\* Danny Kojda, Feng Yi, Karen N. Heinselman, David A. LaVan, Klaus Habicht, Thomas Unold, and Andriy Zakutayev\*



Cite This: <https://doi.org/10.1021/jacs.2c04868>



Read Online

ACCESS |



Metrics & More

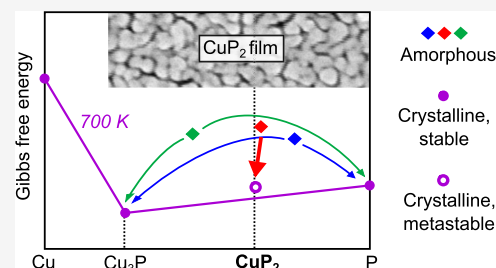


Article Recommendations



Supporting Information

**ABSTRACT:** Numerous phosphorus-rich metal phosphides containing both P–P bonds and metal–P bonds are known from the solid-state chemistry literature. A method to grow these materials in thin-film form would be desirable, as thin films are required in many applications and they are an ideal platform for high-throughput studies. In addition, the high density and smooth surfaces achievable in thin films are a significant advantage for characterization of transport and optical properties. Despite these benefits, there is hardly any published work on even the simplest binary phosphorus-rich phosphide films. Here, we demonstrate growth of single-phase CuP<sub>2</sub> films by a two-step process involving reactive sputtering of amorphous CuP<sub>2+x</sub> and rapid annealing in an inert atmosphere. At the crystallization temperature, CuP<sub>2</sub> is thermodynamically unstable with respect to Cu<sub>3</sub>P and P<sub>4</sub>. However, CuP<sub>2</sub> can be stabilized if the amorphous precursors are mixed on the atomic scale and are sufficiently close to the desired composition (neither too P poor nor too P rich). Fast formation of polycrystalline CuP<sub>2</sub>, combined with a short annealing time, makes it possible to bypass the diffusion processes responsible for decomposition. We find that thin-film CuP<sub>2</sub> is a 1.5 eV band gap semiconductor with interesting properties, such as a high optical absorption coefficient (above 10<sup>5</sup> cm<sup>-1</sup>), low thermal conductivity (1.1 W/(K m)), and composition-insensitive electrical conductivity (around 1 S/cm). We anticipate that our processing route can be extended to other phosphorus-rich phosphides that are still awaiting thin-film synthesis and will lead to a more complete understanding of these materials and of their potential applications.



## INTRODUCTION

Phosphorus readily forms homoelement bonds in the solid state. Accordingly, over 100 phosphorus-rich binary metal phosphides containing both P–P bonds and metal–P bonds have been synthesized in bulk form.<sup>1,2</sup> Often, these compounds have semiconducting properties and decompose into elemental phosphorus and a metal-rich phosphide (with only metal–P bonds) at high temperatures.<sup>2</sup> Thin-film synthesis of P-rich materials would help determine their technological potential and their compatibility with established materials and processes. In addition, growing these materials in thin-film form would be desirable for high-throughput characterization of their properties as a function of composition and process conditions. However, reports of polycrystalline P-rich phosphides as thin films are very scarce and seem to be limited to basic characterization of ZnP<sub>2</sub> and CdP<sub>2</sub> deposited by evaporation of powders of the presynthesized compounds.<sup>3,4</sup> Thin-film growth from elemental or gaseous sources would significantly simplify the synthesis process. However, the high P partial pressure required to stabilize these P-rich compounds poses additional challenges for thin-film growth with respect to bulk synthesis. The classic method of heating the elements in powder form in a sealed ampule cannot easily be extended to phosphorization of metal thin films. Because

the volume of a thin film is very small, it is difficult to achieve a sufficiently high P partial pressure without excessive P recondensation on the film. On the other hand, open-system processes with fixed gas flow rates are more controllable, but the combination of a high P partial pressure, high temperature, and a continuously flowing P source requires careful safety measures.

Like many other P-rich phosphides, bulk synthesis of CuP<sub>2</sub> as a single-crystal or powder is well established,<sup>5–10</sup> but there are no reports of thin-film growth. CuP<sub>2</sub> is a semiconductor that has been proposed as a solar absorber,<sup>11</sup> thermoelectric material,<sup>12,13</sup> electrocatalyst for hydrogen and oxygen evolution,<sup>14</sup> and a component in composite anode materials for Li-<sup>15–17</sup> and Na-based batteries.<sup>18,19</sup> Although CuP<sub>2</sub> has been incorporated in electrochemical devices, its optoelectronic and thermoelectric characterization is incomplete. For example, the optical absorption coefficient of CuP<sub>2</sub> crystals has

Received: May 6, 2022

only been measured in the weak absorption region just above its 1.4–1.5 eV band gap,<sup>8,10</sup> so it is impossible to evaluate its performance as a light absorber in the visible region. For thermoelectric applications, the properties needed to calculate the quality factor  $zT$  have only been measured separately on different  $\text{CuP}_2$  specimens in single-crystal or powder form. A potential method for growing phosphorus-rich phosphide thin films is reactive sputtering. We have recently shown the feasibility of this deposition technique for various metal-rich phosphide compounds.<sup>20–22</sup>

In this work, we present a relatively simple two-step process route to grow polycrystalline  $\text{CuP}_2$  thin films as semiconductors of potential technological interest. First, we deposit amorphous  $\text{CuP}_{2+x}$  by reactive sputtering in a  $\text{PH}_3$ -containing atmosphere. The advantage of this process step is that sufficient P can be incorporated in the films at room temperature at a relatively low  $\text{PH}_3$  partial pressure (0.1 Pa). In the second step, we crystallize the  $\text{CuP}_{2+x}$  films by rapid thermal annealing (RTA) at atmospheric pressure under an inert gas flow. With this two-step process, high phosphorus partial pressures at high temperatures are avoided. We find that the crystallization step must be kinetically facilitated by employing amorphous precursors of sufficiently similar composition to the desired  $\text{CuP}_2$  stoichiometry. We investigate the optical properties of  $\text{CuP}_2$  over a broad spectral range and conduct comprehensive temperature-dependent thermoelectric characterization (including the  $zT$  value) up to room temperature. We find a remarkably high optical absorption coefficient (above  $10^5 \text{ cm}^{-1}$  in the visible region), low thermal conductivity ( $1.1 \text{ W}/(\text{K m})$ ), composition-insensitive electrical conductivity ( $1 \text{ S/cm}$ ), and a moderate native doping density ( $10^{15}–10^{17} \text{ cm}^{-3}$ ) potentially suitable for photovoltaic applications.

## RESULTS AND DISCUSSION

**Structure and Bonding.** Bonding in  $\text{CuP}_2$  has some interesting features that are worth a brief analysis. Bulk  $\text{CuP}_2$  crystallizes in the monoclinic structure shown in Figure 1, with

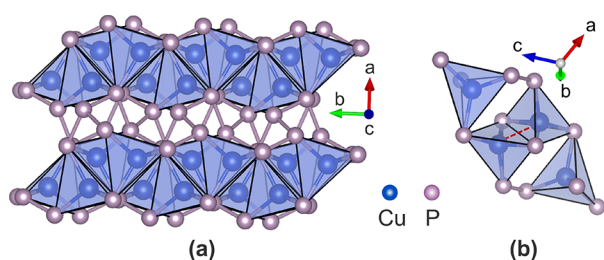


**Figure 1.** Monoclinic  $P2_1/c$  structure of  $\text{CuP}_2$ . (a) View emphasizing the sheets of  $\text{CuP}_4$  tetrahedra and of single-bonded P atoms. (b) View emphasizing the short Cu–Cu distance (dashed line) between two edge-sharing  $\text{CuP}_4$  tetrahedra.<sup>23</sup>

space group  $P2_1/c$ .<sup>7</sup> The structure consists of alternating sheets of  $\text{CuP}_4$  tetrahedra and of homoelement-bonded P atoms in planes parallel to (100) (Figure 1). Each  $\text{CuP}_4$  tetrahedron shares an edge and three corners with other analogous tetrahedra. The existence of anion–anion bonding is a key qualitative difference between P-rich compounds like  $\text{CuP}_2$  and most optoelectronic compounds such as III–V and II–VI semiconductors. The generalized  $8 - N$  rule<sup>24</sup> can then be used to interpret bonding. In this framework, one may assign the  $-1$  oxidation state to one-half of the P atoms, since they

are bonded to two other P atoms and three Cu atoms. The remaining P atoms have three P–P bonds and one Cu–P bond and are formally neutral, as the three homoelement bonds complete their octet. To achieve charge neutrality, Cu should then be in the  $+1$  oxidation state. While explicit calculations<sup>12</sup> indicate that only about 30% of this charge is actually transferred to P due to significant covalency, they also confirm that the charge is only accepted by the P atoms that are in the  $-1$  oxidation state. Thus,  $\text{CuP}_2$  is a relatively rare example of a compound with mixed anion valence.

Another peculiar feature of the  $P2_1/c$  structure of  $\text{CuP}_2$  is that pairs of Cu atoms are quite close to each other ( $2.48 \text{ \AA}$ ).<sup>7</sup> Comparing this distance to the bond length of metallic Cu ( $2.55 \text{ \AA}$ ) and the metallic radius of single-bonded Cu ( $2.49 \text{ \AA}$ )<sup>25</sup> suggests that some metallic Cu–Cu bonding is to be expected. This is confirmed by calculation of a nonzero electron localization function between the two Cu atoms and by experimental analysis of phonon modes in  $\text{CuP}_2$ .<sup>26</sup> These Cu–Cu dimers were recently shown to vibrate anharmonically as a rattling mode and strongly scatter acoustic phonons.<sup>26</sup> This is the key feature enabling low lattice thermal conductivity in  $\text{CuP}_2$  in spite of its relatively high acoustic conductivity, thus making it interesting for thermoelectrics.

**Synthesizability.**  $\text{CuP}_{2+x}$  thin films with a broad range of  $x$  (positive and negative) could be deposited by reactive sputtering in a  $\text{PH}_3/\text{Ar}$  atmosphere at room temperature by using either a Cu target, a  $\text{Cu}_3\text{P}$  target, or both at the same time (see the Experimental Details and the  $x$ -axis in Figure 2a). The main available parameters to tune  $x$  are the RF power on the targets and the  $\text{PH}_3$  partial pressure (see the Supporting Information). Decreasing the power led to higher P contents due to a more P-enriched target surface and/or to a lower flux of Cu at the substrate, promoting phosphorization at the substrate. Higher  $\text{PH}_3$  partial pressures can be achieved by increasing the total pressure or the  $\text{PH}_3$  concentration in Ar. Because the  $\text{PH}_3$  concentration was limited to below 5% in our setup, we had to employ a relatively high sputter pressure ( $2 \text{ Pa} \approx 15 \text{ mTorr}$ ) to obtain films of  $\text{CuP}_2$  stoichiometry. The wide tunability of the P content in Cu–P films was also observed in our recently reported amorphous B–P films by reactive sputtering.<sup>21</sup> This compositional flexibility is likely related to the ability of P to form homoelement bonds in the films and segregate as an elemental impurity. Hence, we assume that the excess P in  $\text{CuP}_{2+x}$  films with  $x > 0$  is mainly bonded to other P atoms.

As-deposited  $\text{CuP}_{2+x}$  films did not exhibit any X-ray diffraction (XRD) peaks (Figure S2), so we crystallized them in an RTA furnace at atmospheric pressure under a  $\text{N}_2$  flow. Loss of phosphorus at moderate temperatures is a well-known phenomenon in many P-rich phosphides.<sup>2</sup> We also observed P losses in all our postannealed  $\text{CuP}_2$  films (Figure 2a,b). However, the dependence of these P losses on the initial composition of the as-deposited films is not trivial.

In Figure 2a, we compare the P/Cu ratio before and after annealing at  $400 \text{ }^\circ\text{C}$  for 5 min for various initial compositions between  $\text{CuP}_{1.3}$  and  $\text{CuP}_{4.5}$ . The P/Cu ratio is measured by X-ray fluorescence (XRF) so it represents an average through the depth of the film. Several interesting trends can be identified. First, thicker films generally experience milder P losses because P located deeper in the film requires a longer time to diffuse out. Second, sufficiently thick films with initial composition in the  $\text{CuP}_{2.2}–\text{CuP}_{2.7}$  range can be “locked” into the desired  $\text{CuP}_2$  stoichiometry by annealing (Figure 2b). Third, films with

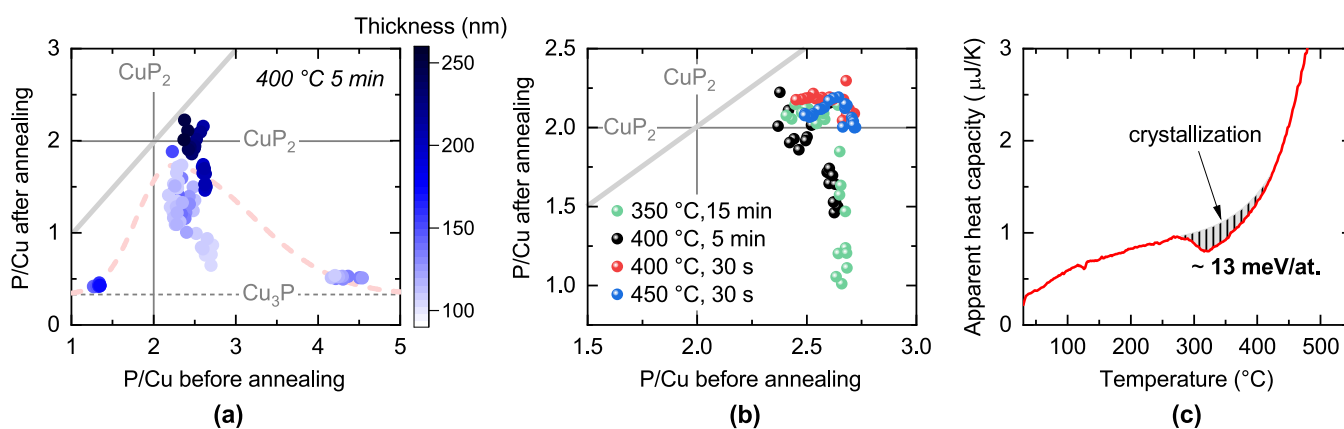


**Figure 2.** Effect of postannealing on amorphous  $\text{CuP}_{2+x}$  films. (a) Change in P/Cu ratio after annealing for films of different initial compositions and thicknesses under constant annealing conditions ( $400\text{ }^\circ\text{C}$  for 5 min). Vertical and horizontal lines indicate the  $\text{CuP}_2$  and  $\text{Cu}_3\text{P}$  stoichiometries. The gray diagonal line corresponds to P/Cu ratios that are not modified by annealing. The dashed line is a guide to the eye, indicating that the films with initial composition closest to  $\text{CuP}_2$  are the ones with least severe P losses. (b) Change in P/Cu ratio after annealing for films of  $\text{CuP}_{2.4}$ – $\text{CuP}_{2.7}$  initial composition and similar thicknesses under different annealing conditions. (c) Calorimetry experiment on an initially amorphous 90 nm thick  $\text{CuP}_{2.5}$  film deposited on a  $\text{Si}_3\text{N}_4$  membrane. If we assume a baseline for the heat capacity as shown in the figure, the energy released in the  $300$ – $400\text{ }^\circ\text{C}$  region (area under the baseline) is estimated as 13 meV/atom.

severe P losses tend to approach the  $\text{Cu}_3\text{P}$  composition after annealing.  $\text{Cu}_3\text{P}$  is the most commonly reported binary stoichiometry in the Cu–P system.<sup>5,6,27,28</sup>

Last, and most surprisingly, we find that highly P-rich initial compositions do not help achieve a higher P content in the postannealed films. In fact, the opposite is true. When the initial composition is in the (P-rich)  $\text{CuP}_{4.1}$ – $\text{CuP}_{4.5}$  range, the postannealed composition is around  $\text{CuP}_{0.5}$  (Figure 2a). When the initial composition is much poorer in P ( $\text{CuP}_{1.3}$ – $\text{CuP}_{1.4}$  range), the postannealed composition is similar, around  $\text{CuP}_{0.4}$  (Figure 2a). On the other hand, when the initial composition is in an intermediate  $\text{CuP}_{2.2}$ – $\text{CuP}_{2.7}$  range closer to the desired  $\text{CuP}_2$  stoichiometry, P losses upon annealing are much slower in films of comparable thickness.

Using these atomically dispersed precursors with moderate P excess with respect to the target  $\text{CuP}_2$  stoichiometry, the necessary species for forming crystalline  $\text{CuP}_2$  are readily available within a subnanometer distance of their ideal crystallographic site. This enables fast crystallization of monoclinic  $\text{CuP}_2$ . On the other hand, solid-state diffusion processes responsible for P losses have longer characteristic lengths, on the order of the film thickness (in our case, hundreds of nanometers). Thus, there is an optimal annealing time that is sufficient for  $\text{CuP}_2$  to crystallize but insufficient for substantial P losses to occur. Presumably, the lower total energy achieved by crystallizing the originally amorphous  $\text{CuP}_2$  film (Figure 2c) also helps delay P evaporation.

Conversely, precursor films that are too P-rich require solid-state diffusion to form a crystalline  $\text{CuP}_2$  phase because Cu atoms are too far apart in the initial amorphous phase. This Cu diffusion process now competes with the unwanted P diffusion leading to P evaporation. As a result, P losses are much faster. These findings are summarized in the qualitative diagram shown in Figure 3.

To visualize the P loss process, we image a film with final composition  $\text{CuP}_{1.3}$  by scanning electron microscopy (SEM, Figure 4). Two phases can be clearly distinguished on the micrometer scale: a porous polycrystalline matrix with grain size around 30 nm and islands of more compact morphology. The intensity ratio between the Cu and the P peaks in energy-

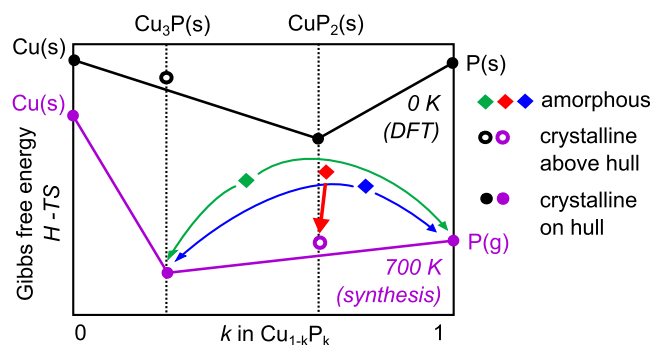


**Figure 3.** Qualitative convex hull of the Cu–P system at two different temperatures. Among competing phases, only  $\text{Cu}_3\text{P}$  and the elements are considered. At 0 K, the Gibbs free energy only consists of enthalpy  $H$ , so the convex hull is drawn following DFT enthalpy calculations as available on the Materials Project database.<sup>27</sup>  $\text{CuP}_2$  is found to be a stable phase (on the convex hull), and  $\text{Cu}_3\text{P}$  is slightly metastable (above the convex hull). At 700 K, our experiments indicate that  $\text{CuP}_2$  is destabilized. Part of the reason may be a large entropic term  $TS$  for elemental P, which is in gaseous form at this temperature. When higher energy amorphous precursors (diamond data points) are rapidly heated to 700 K, decomposition into  $\text{Cu}_3\text{P}$  and gaseous P is thermodynamically favored. However,  $\text{CuP}_2$  formation is kinetically facilitated when the initial composition of the precursors is sufficiently close to the  $\text{CuP}_2$  stoichiometry (red diamond).

dispersive X-ray spectroscopy (EDX) increases by a factor  $\sim 5.5$  when moving from the matrix to the islands (Figure S1). Thus, we conclude that the matrix consists of  $\text{CuP}_2$  and the islands consist of  $\text{Cu}_3\text{P}$ . The mechanism of conversion from  $\text{CuP}_2$  to  $\text{Cu}_3\text{P}$  appears to be diffusion of Cu in the plane of the substrate, contributing to the enlargement of seed  $\text{Cu}_3\text{P}$  islands. At the same time, P gradually evaporates elsewhere. Because the most stable gaseous form of phosphorus<sup>29</sup> at our annealing temperatures is  $\text{P}_4$  and no intermediate solid phases between  $\text{CuP}_2$  and  $\text{Cu}_3\text{P}$  are observed, the  $\text{CuP}_2$  decomposition reaction can be written as  $12\text{CuP}_2(\text{s}) \rightarrow 4\text{Cu}_3\text{P}(\text{s}) + 5\text{P}_4(\text{g})$ .

Figure 2b shows the effect of annealing temperature and time on the final composition. As expected, increasing the annealing time at fixed temperature results in more severe P

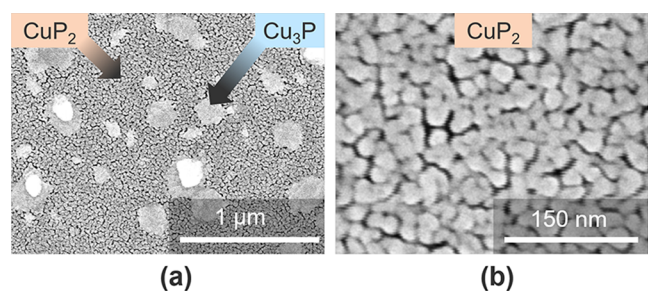


**Figure 4.** Morphology of a postannealed film with overall  $\text{CuP}_{1.3}$  composition. (a) Low-magnification SEM image showing a dual-phase morphology with a  $\text{CuP}_2$  matrix and  $\text{Cu}_3\text{P}$  islands. (b) High-magnification SEM image showing porosity in the  $\text{CuP}_2$  matrix. Phase identification was performed on the basis of spatially resolved EDX spectra (Figure S1).

losses (compare the data from 30 s versus 5 min annealing time at  $400^\circ\text{C}$ ). In general, longer annealing times can be tolerated at lower annealing temperatures. For example, annealing at  $350^\circ\text{C}$  for 15 min yields about as many P-poor samples as the case of annealing at  $400^\circ\text{C}$  for 5 min. Note that the spread of final P/Cu ratios sometimes obtained for films of otherwise similar initial P/Cu ratios, and the thicknesses is mainly caused by the different positions of the samples inside the furnace. The samples located further downstream with respect to the gas flow tend to lose less P, possibly because they are exposed to a finite P partial pressure due to P evaporating from the samples further upstream.

We observe a decrease in the apparent heat capacity of an as-deposited  $\text{CuP}_{2.5}$  film at around  $300^\circ\text{C}$  by nanocalorimetry (Figure 2c). This indicates an exothermic signal, which may be related to the transition from the amorphous to the (more stable) polycrystalline state. The heat capacity baseline needed to calculate the heat of crystallization is not straightforward to define. If we assume the baseline shown in Figure 2c, we estimate the crystallization energy of  $\text{CuP}_2$  as 13 meV/atom. Although the uncertainty on this value is substantial, some qualitative conclusions can still be drawn. The calculated formation enthalpy of  $\text{CuP}_2$  from the elements in their standard state is 112 meV/atom.<sup>27</sup> Because this value is much larger than the estimated crystallization energy, most of the formation energy has probably already been released during formation of the amorphous compound. The thermal energy of a solid at  $400^\circ\text{C}$  is approximately  $3kT = 174$  meV/atom by using the Dulong–Petit law. Thus, the extra stabilization achieved by crystallizing  $\text{CuP}_2$  is only a small fraction of the thermal energy available at that temperature.

It is also interesting to consider typical values for the calculated energy difference between the most stable amorphous configuration and most stable crystalline polymorph for a given material. This quantity has been calculated in a previous study for 41 material systems (mainly oxides) at 0 K.<sup>30</sup> The energy difference varies between  $\sim 50$  and  $\sim 500$  meV/atom depending on the material. The significantly lower crystallization energy measured in  $\text{CuP}_2$  could indicate that the entropic contribution to the total energy is substantially higher in the amorphous state than in the crystalline state at finite temperatures. Higher entropy is indeed expected in the amorphous state due to higher disorder, and it would contribute to reducing the energy difference between the amorphous and crystalline state of  $\text{CuP}_2$  at  $\sim 700$  K with respect to 0 K. Although this explanation is plausible, it is also

possible that  $\text{CuP}_2$  and other non-oxide compounds simply exhibit different energetic trends than the computationally investigated selection of compounds. Computational analysis of the energetics of a more diverse range of amorphous material systems would certainly be useful.

**Stability.** Previous work on  $\text{CuP}_2$  single crystals does not comment on their stability under ambient conditions. On the basis of simple observations on our thin-film samples, we suggest that the air stability of  $\text{CuP}_2$  should be further investigated. A change in color is consistently observed in as-deposited  $\text{CuP}_{2+x}$  after few hours of exposure to ambient air, signaling a reaction that is not limited to a surface layer of a few nanometers thickness. For this reason, the films characterized in this work were annealed immediately after deposition. After annealing, the bulk properties of the films appear to be stable for a longer time (at least a few days) under ambient conditions, as judged by their visual appearance and electrical conductivity. The higher reactivity of amorphous  $\text{CuP}_{2+x}$  may be due to the extra P present before annealing and to the higher energy associated with the amorphous state (Figure 2c). Both the amorphous and the polycrystalline films appear to be stable in a  $\text{N}_2$  atmosphere.

After either type of film has been exposed to air for a sufficiently long time, the reaction front has reached the back surface of the film, as evident by visual inspection through the glass substrate. The exact details of the  $\text{CuP}_{2+x}$ –air reaction are currently unknown. However, XRF measurements reveal a large decrease in P/Cu ratio after prolonged exposure to air, indicating that the reaction involves P losses. We suspect that the high sputter pressure (2 Pa) necessary to obtain a P/Cu ratio above 2 in our growth setup may explain why the reaction of  $\text{CuP}_2$  films with air is not limited to a surface layer. Films sputtered at high pressure are generally more porous and more air sensitive due to their higher surface area.<sup>31</sup> Thus, we cannot conclude that  $\text{CuP}_2$  films are intrinsically unstable in air. The stability of  $\text{CuP}_2$  films sputtered at lower pressures or deposited by other techniques should be investigated to clarify this issue.

**Structural and Vibrational Properties.** In agreement with nanocalorimetry results, the originally amorphous  $\text{CuP}_{2+x}$  films only begin to show crystalline XRD peaks above  $300^\circ\text{C}$  annealing temperature (Figure S2). Beyond this lower limit, it is possible to obtain polycrystalline  $\text{CuP}_{2+x}$  films in the  $P2_1/c$  structure under various annealing conditions. As long as the final composition is close to the nominal  $\text{CuP}_2$  stoichiometry, XRD patterns of films processed under different annealing conditions are rather similar (Figure S2). As an example, the XRD pattern of a  $\text{CuP}_2$  film annealed at  $450^\circ\text{C}$  for 30 s (Figure 5a) contains all the peaks expected for the  $P2_1/c$  structure, without major preferential orientation effects and without clear peaks from secondary phases above the noise level. The XRD peak positions closely match the positions of the reference bulk  $\text{CuP}_2$  sample,<sup>7</sup> indicating that structural parameters (including the short Cu–Cu distance) are about the same in thin-film and bulk  $\text{CuP}_2$ . XRD peaks from  $\text{Cu}_3\text{P}$  in the hexagonal  $P6_3cm$  structure are observed in  $\text{CuP}_{2+x}$  films when  $x < 0$  (Figure S2). However, the threshold value of  $x$  at which  $\text{Cu}_3\text{P}$  peaks begin to appear strongly varies with annealing conditions. When  $x > 0$  (P-rich films), no XRD peaks associated with secondary phases like  $\text{Cu}_2\text{P}_7$  or elemental phosphorus are observed up to the most P-rich composition reached in this study ( $\text{CuP}_{2.2}$ ).

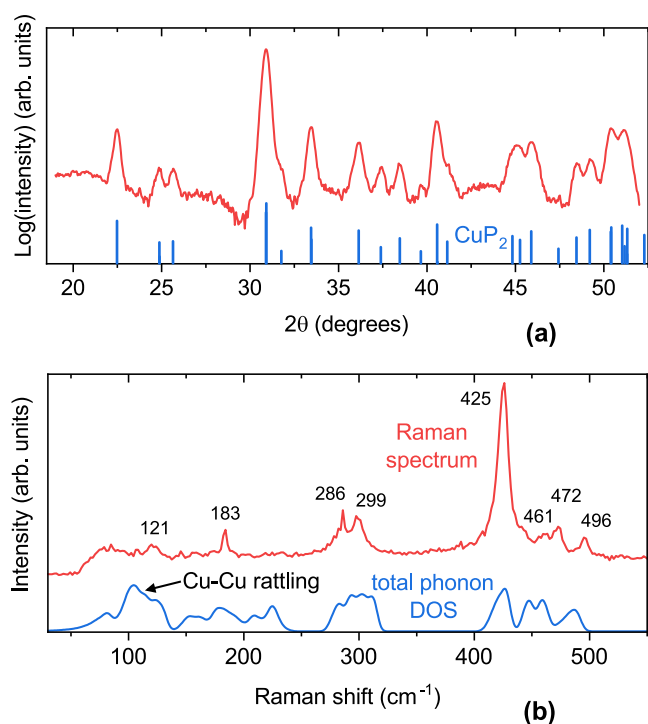


**Figure 5.** Structural and vibrational characterization of a film with  $\text{CuP}_2$  stoichiometry after postannealing at  $450^\circ\text{C}$  for 30 s. (a) Experimental XRD pattern together with the reflections expected for randomly oriented  $\text{CuP}_2$  in the monoclinic  $P2_1/c$  structure.<sup>7</sup> XRD patterns under other annealing conditions are shown in Figure S2. (b) Experimental Raman spectrum with labels for the identified peak positions. The total phonon density of states of  $\text{CuP}_2$  in the  $P2_1/c$  structure, as calculated in the Materials Project database,<sup>27</sup> is also shown. The Cu–Cu rattling mode ( $\sim 100\text{ cm}^{-1}$ ) believed to limit the thermal conductivity of  $\text{CuP}_2$ <sup>26</sup> is indicated.

It might be tempting to conclude that single-phase  $\text{CuP}_{2+x}$  can be grown over a wide  $x$  range, in which defect formation is favored over secondary phase precipitation. However, secondary phases in amorphous form (not detected by XRD) are likely to be present in our samples for the following reasons. First, amorphous secondary phases were identified in a

previous study on the phase equilibrium between  $\text{Cu}_3\text{P}$  and  $\text{CuP}_2$  in powder form.<sup>32</sup> This observation rendered XRD-determined phase boundaries incorrect. Second, our short annealing times may not be sufficient to crystallize phases with a significantly different composition than the original precursors. In fact,  $\text{Cu}_3\text{P}$  can only form if  $\text{CuP}_2$  loses more than 80% of its original P in some regions of the film. If the annealing process is stopped before these losses can take place, and if there are no stable phases between  $\text{CuP}_2$  and  $\text{Cu}_3\text{P}$ , the likely result is formation of amorphous phases with intermediate composition. Third, the electrical conductivity of our films is roughly constant in the  $\text{CuP}_{1.0}$ – $\text{CuP}_{2.2}$  composition range (Figure 6a). It is improbable that the high defect densities required to accommodate this non-stoichiometry do not have any effect on the electrical properties. Thus, electrically inactive secondary phases (such as the disconnected  $\text{Cu}_3\text{P}$  islands shown in Figure 4a) are very likely to coexist with point defects in highly nonstoichiometric  $\text{CuP}_2$ .

The Raman spectrum of the same sample used for XRD characterization is plotted in Figure 5b. The phonon density of states (DOS) of  $\text{CuP}_2$ , as calculated by density functional perturbation theory in good agreement with recent experiments,<sup>26</sup> is also shown for comparison.<sup>27,33,34</sup> Because Raman spectra of bulk  $\text{CuP}_2$  are not available in the literature, we briefly discuss some qualitative aspects here. Raman features originating from the phonon bands centered around 300 and  $450\text{ cm}^{-1}$  can clearly be seen in the experimental spectrum. In particular, the most intense Raman peak at  $425\text{ cm}^{-1}$  probably arises from one of the lowest-energy phonon branches within the highest-energy band in the calculated DOS. All modes in this band essentially involve vibrations of P atoms with nearly static Cu atoms. The lower the phonon energy, the larger the contribution from Cu vibrations, as expected from the larger mass of Cu.

Because the film is polycrystalline, there are selection rules for Raman-active phonon modes and the Raman spectrum will not directly reflect the phonon DOS. Specifically, all atoms in  $\text{CuP}_2$  are at 4e Wyckoff positions of the  $P2_1/c$  space group, so only the  $A_g$  and  $B_g$  modes are Raman-active according to the character tables.<sup>35</sup> With a 12-atom unit cell, 18 Raman-active modes are predicted in total.<sup>35</sup> Eight peaks can be identified

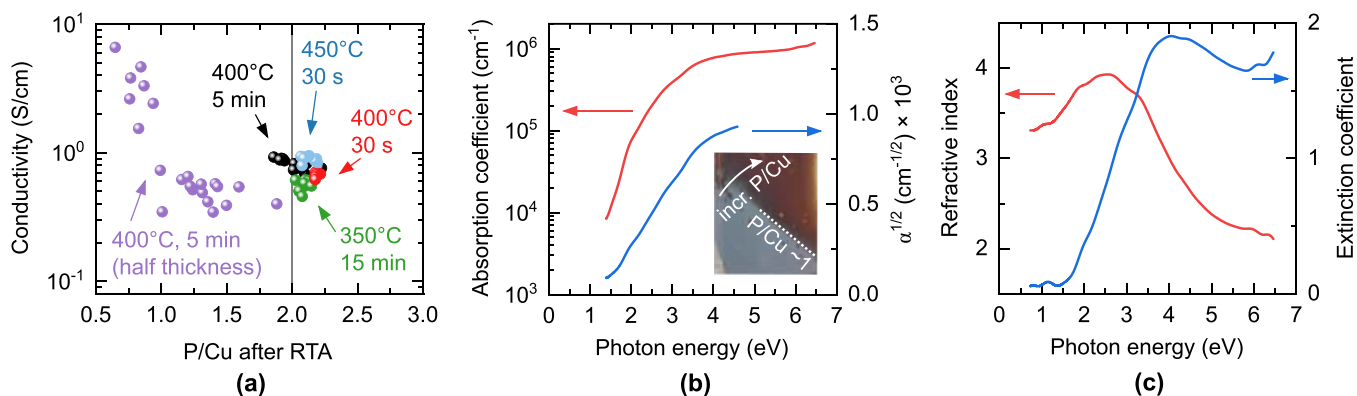


**Figure 6.** Room-temperature electrical and optical properties of postannealed  $\text{CuP}_{2+x}$  films. (a) Electrical conductivity as a function of composition (measured after annealing) and annealing conditions. Films are of comparable thickness except for the P-poor purple data points, which have about half the thickness as the other ones. A zoomed-in view around the  $\text{CuP}_2$  stoichiometry is available in Figure S4. (b) Absorption coefficient  $\alpha$  of a postannealed  $\text{CuP}_{2.0}$  film together with a  $\alpha^{1/2}$  plot versus photon energy. Inset: photograph of a film with increasing P/Cu ratio from bottom left to top right. When the P/Cu ratio decreases below roughly 1, the appearance of the film changes from dark red (characteristic of semiconducting  $\text{CuP}_2$ ) to gray (characteristic of metallic  $\text{Cu}_3\text{P}$ ). (c) Refractive index and extinction coefficient of the same  $\text{CuP}_{2.0}$  film shown in (b).

the experimental spectrum (Figure 5b). The Cu–Cu rattling mode identified by Qi et al. as an important scatterer of heat-transporting phonons<sup>26</sup> is either symmetry-forbidden or too low in intensity to be distinguished by Raman spectroscopy.

**Electrical and Optical Properties.** The room-temperature electrical conductivity of postannealed polycrystalline films in the  $\text{CuP}_{2.0}$ – $\text{CuP}_{2.2}$  composition range is between 0.5 and 1.0 S/cm at room temperature, without a clear dependence on the P/Cu ratio (Figure 6a). The conductivity slightly increases with increasing annealing temperature, regardless of annealing time (Figure S4). Previously reported conductivities of  $\text{CuP}_2$  single crystals range from 0.01 to 30 S/cm, presumably due to differences in the crystal quality.<sup>6,8–10</sup> Films with severe P losses have significantly higher conductivities (Figure 6a), probably due to percolation paths between highly conductive  $\text{Cu}_3\text{P}$  phases.<sup>6</sup> The Seebeck coefficient measured on a freshly annealed  $\text{CuP}_{2.0}$  film is  $+390(10)$   $\mu\text{V}/\text{K}$  (Figure S3), indicating native p-type doping. All previously reported  $\text{CuP}_2$  single crystals were also p-type with higher Seebeck coefficients in the 690–820  $\mu\text{V}/\text{K}$  range. The work function, measured with a Kelvin probe in air on a freshly annealed  $\text{CuP}_{2.0}$  film, is 5.0(1) eV.

$\text{CuP}_2$  is a relatively strong absorber of light. Its absorption coefficient  $\alpha$  reaches  $10^5 \text{ cm}^{-1}$  at a photon energy  $h\nu = E_g + 0.6$  eV above its band gap  $E_g = 1.5(1)$  eV (Figure 6b). This compares favorably even with the most efficient direct gap photovoltaic absorbers such as GaAs, CdTe, and  $\text{CH}_3\text{NH}_3\text{PbI}_3$  (MAPI).<sup>36</sup> In fact, the absorption coefficient is as high as in some exciton-enhanced photoabsorbers such as  $\text{BiI}_3$  and  $\text{Cu}_2\text{BaSnS}_4$ ,<sup>37,38</sup> indicating that  $\text{CuP}_2$  may deserve more detailed optoelectronic characterization.

We find that  $\alpha^{1/2}$  is linear in photon energy over a 2 eV spectral range above the band gap (Figure 6b), indicating that  $\alpha \propto (h\nu - E_g)^2$ . Both the estimated band gap and the spectral dependence of the absorption coefficient are in agreement with previous work on  $\text{CuP}_2$  single crystals.<sup>8–10</sup> Because the  $\alpha \propto (h\nu - E_g)^2$  behavior is often associated with an indirect gap in conventional semiconductors,<sup>39</sup> an indirect gap was previously assumed for these  $\text{CuP}_2$  crystals.<sup>8,10</sup>

However, there are at least two other factors to consider. (1) The absorption strength of  $\text{CuP}_2$  is high even for a direct gap material, so indirect transitions are unlikely to be responsible for it. (2) According to the calculated band structure of  $\text{CuP}_2$ ,<sup>27</sup> the fundamental gap should be direct and located between the  $\Gamma$  and the Y point of the Brillouin zone. Two indirect gaps with slightly higher energies exist due to additional valence band pockets at the X point and between the Y and H points.<sup>27</sup> Even though we observe an  $\alpha \propto (h\nu - E_g)^2$  behavior, care should be taken when employing the absorption characteristics typical of group IV and III–V semiconductors to interpret the nature of the optical transitions of other semiconductors with substantially different band structures. A clear difference between  $\text{CuP}_2$  and conventional semiconductors is that the former has many valence and conduction band pockets at different points of the Brillouin zone. Hence, many different optical transitions can contribute to the overall absorption coefficient.

The refractive index of  $\text{CuP}_2$  is 3.3–3.4 in the transparent region (Figure 6c). Extrapolation of the real part of the dielectric function to zero photon energy (Figure S5) yields a high-frequency permittivity  $\epsilon_\infty = 10.5 \pm 1.0$ . Interestingly, there seems to be a critical P/Cu ratio close to 1, where the electrical and optical properties shift from being “ $\text{CuP}_2$ -like”

(semiconducting and IR transparent) to being “ $\text{Cu}_3\text{P}$ -like” (metallic and opaque). This transition is manifested by an abrupt change in conductivity (Figure 6a) and visual appearance (inset of Figure 6b).

**Thermoelectric Characterization.** We conducted DC and double AC Hall effect measurements as well as temperature-dependent thermoelectric characterization of three films. They have the following compositions:  $\text{Cu}_{2.50}\text{P}$  (labeled “ $\text{Cu}_{3-z}\text{P}$ ”),  $\text{Cu}_{1.61}\text{P}$ , and  $\text{CuP}_{1.35}$  (labeled “ $\text{CuP}_{2-y}$ ”). We use these labels to emphasize similarity to  $\text{Cu}_3\text{P}$  and  $\text{CuP}_2$  as discussed in the previous section. This set of films was deposited on  $\text{Si}_3\text{N}_4$  membranes as part of a microchip-based thin-film transport characterization platform.<sup>40</sup> Differences between this set of films and the films deposited on glass characterized in the rest of the article are listed in the Supporting Information. Because these films have intermediate compositions between  $\text{CuP}_2$  and  $\text{Cu}_3\text{P}$ , their properties may be influenced by inhomogeneity, as exemplified by the dual-phase morphology shown in Figure 4. Nevertheless, important qualitative trends in the transport properties of these films as a function of composition can still be discerned.

The temperature dependence of the electrical conductivity (Figure 7a) suggests that  $\text{CuP}_{2-y}$  is a nondegenerately doped semiconductor and that the two other films are either metallic or degenerately doped semiconductors. Hall effect measure-

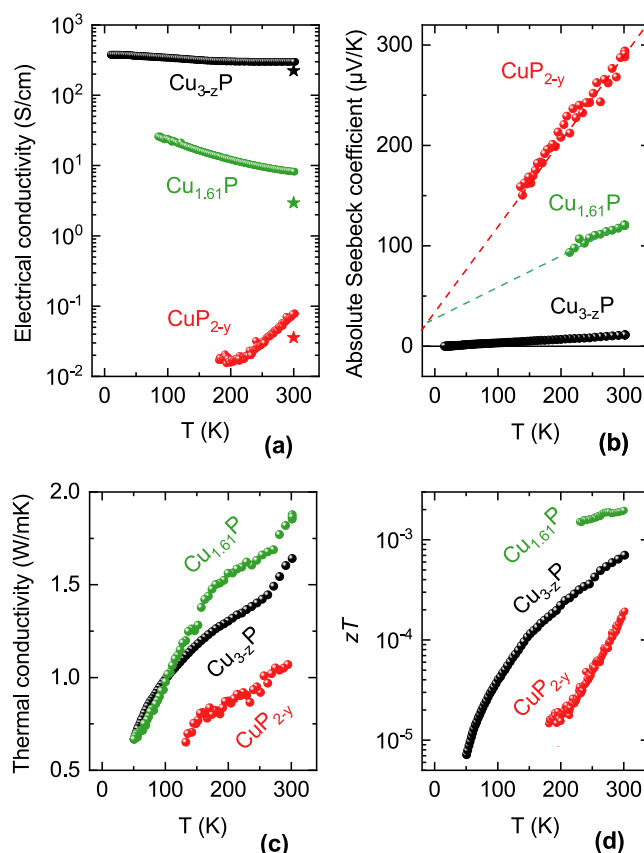


**Figure 7.** Thermoelectric properties of three postannealed Cu–P films as a function of temperature  $T$ . The compositions after annealing are indicated. (a) Electrical conductivity  $\sigma$ , which was also remeasured at room temperature one month after the temperature-dependent measurement (star markers). (b) Absolute Seebeck coefficient  $S \equiv S_{\text{Cu-P}}$ , with linear trends indicated. (c) Thermal conductivity  $\kappa$ . (d) Thermoelectric figure of merit  $zT = \sigma S^2 T / \kappa$ .

ments at room temperature confirm this interpretation (Figure 8), with high carrier concentrations measured in  $\text{Cu}_{3-z}\text{P}$  and

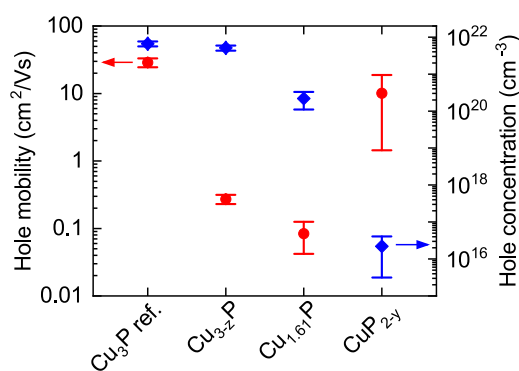


**Figure 8.** Hole mobility and concentration by double AC Hall effect measurements on the same Cu–P films shown in Figure 7. The film labeled “ $\text{Cu}_3\text{P ref.}$ ” is a continuous polycrystalline  $\text{Cu}_3\text{P}$  film deposited by reactive sputtering at 360 °C and used as a reference.

$\text{Cu}_{1.61}\text{P}$  (above  $10^{20} \text{ cm}^{-3}$ ) and a moderate carrier concentration measured in  $\text{CuP}_{2-y}$  ( $10^{15}$ – $10^{17} \text{ cm}^{-3}$ ). All films have a positive Hall voltage confirming their p-type conductivity. Note that the conductivity of  $\text{Cu}_{1.61}\text{P}$  and  $\text{CuP}_{2-y}$  after one month of storage is appreciably lower (Figure 7a), highlighting possible stability issues as discussed in the previous sections.

Because of the inverse relationship between carrier concentration and thermovoltage,<sup>41</sup> the Seebeck coefficient is highest in  $\text{CuP}_{2-y}$  and lowest in  $\text{Cu}_{3-z}\text{P}$  (Figure 7b). Interestingly, the Seebeck coefficient increases linearly with temperature in all three films (Figure 7b). This behavior is often a sign of a temperature-independent carrier concentration,<sup>41</sup> a typical feature of materials with nonzero density of states at the Fermi level (i.e., metals and degenerate semiconductors such as  $\text{Cu}_{3-z}\text{P}$  and  $\text{Cu}_{1.61}\text{P}$ ). However, a linear increase of the Seebeck coefficient with temperature is not readily explained for a more weakly doped semiconductor like  $\text{CuP}_{2-y}$ . In an ideal scenario, we would expect the carrier concentration to increase with temperature due to increasing defect ionization and the Seebeck coefficient to decrease accordingly. The reason for this discrepancy is unclear. One could invoke the role of film inhomogeneity due to the presence of  $\text{Cu}_3\text{P}$  secondary phases (Figure 4) or assume that the increase of electrical conductivity with temperature (Figure 7a) is due to mobility changes rather than to the hole concentration changes. Yet, a simultaneous increase in hole concentration and Seebeck coefficient with temperature was reported for  $\text{CuP}_2$  single crystals,<sup>8</sup> where inhomogeneity effects can be excluded. Multiband transport could also cause an unusual temperature behavior due to increasing contributions from the additional valence band pockets of  $\text{CuP}_2$  with increasing temperature. However, application of the Boltzmann transport equation<sup>42</sup> on the calculated  $\text{CuP}_2$  band structure<sup>27</sup> reveals that a significant decrease in the Seebeck coefficient is expected in the 200–300 K range assuming a concurrent increase in hole concentration by 1 order of magnitude (Figure S6).

As another hypothesis, one could assume that  $\text{CuP}_{2-y}$  is highly compensated by donor defects at low temperatures, but its p-type character becomes more dominant at higher temperatures due to activation of a deeper acceptor. If this hypothesis is correct, one would expect both the electrical

conductivity and the Seebeck coefficient to increase with temperature as we experimentally observe—the former due to an increase in the concentration of ionized acceptors and the latter due to a decreasing contribution from the (negative) n-type Seebeck coefficient.<sup>41</sup> Previous work also suggested the possibility of charge compensation in  $\text{CuP}_2$  single crystals based on the temperature dependence of their carrier mobility.<sup>10</sup> The position of the acceptor level in our  $\text{CuP}_{2-y}$  film can be estimated as 121(3) meV above the valence band from an Arrhenius plot of the electrical conductivity in the 230–300 K temperature range (Figure S7).

The room-temperature thermal conductivity of  $\text{CuP}_{2-y}$  is 1.1 W/(K m) (Figure 7c). This value is lower than in  $\text{CuP}_2$  single crystals (3.6–4.7 W/(K m) depending on lattice direction)<sup>26</sup> as may be expected for a polycrystalline sample. Our measured conductivity is, however, in excellent agreement with the calculated 1.12 W/(K m) amorphous limit for bulk  $\text{CuP}_2$ .<sup>12</sup> The increasing thermal conductivity with increasing temperature is unlike the  $\propto 1/T$  behavior typical of crystalline semiconductors in this temperature range. Instead, it is often observed in amorphous or highly disordered materials, consistent with the observation that our measured conductivity is very close to the amorphous limit. On the basis of these results, we assume that the phonon mean free path in the  $\text{CuP}_{2-y}$  film is low due to disorder<sup>43</sup> and/or phonon boundary scattering.<sup>44</sup> The latter is likely enhanced by the small grains, low thickness, and porous morphology of the film.<sup>43–45</sup> The electronic contribution to the thermal conductivity is negligible due to the low hole concentration of  $\text{CuP}_{2-y}$  (Figure 8). The thermal conductivities of  $\text{Cu}_{3-z}\text{P}$  and  $\text{Cu}_{1.61}\text{P}$  are only slightly higher and their temperature dependences are similar to the case of  $\text{CuP}_{2-y}$ . Thus, we conclude that the thermal conductivity is phonon-mediated and strongly limited by film morphology in all three films. In fact, scattering of charge carriers (holes) is also morphology-limited. The hole mobility of the present  $\text{Cu}_{3-z}\text{P}$  film ( $0.27 \text{ cm}^2/(\text{V s})$ ) is 2 orders of magnitude lower than in a continuous  $\text{Cu}_3\text{P}$  film on glass with about the same carrier concentration ( $28.8 \text{ cm}^2/(\text{V s})$ , see Figure 8).

$\text{CuP}_2$  has recently been proposed as a potential thermoelectric material.<sup>12,13</sup> Our measurements on a  $\text{CuP}_{2-y}$  film confirm that the lattice contribution to its thermal conductivity is indeed sufficiently low for thermoelectric applications. However, the thermoelectric figure of merit  $zT$  at room temperature is still low for all investigated compositions (Figure 7d) due to low power factors (Figure S8). In the vicinity of the  $\text{Cu}_3\text{P}$  stoichiometry, the main issue is a low Seebeck coefficient. In the vicinity of the  $\text{CuP}_2$  stoichiometry, the main issue is low electrical conductivity. Even taking the more favorable properties of our  $\text{CuP}_2$  films on glass (Table 1) or of previously reported  $\text{CuP}_2$  single crystals,<sup>8</sup> the  $zT$  value at room temperature would only be 0.004 and 0.05, respectively. It might be possible to optimize the hole concentration of  $\text{CuP}_2$  by extrinsic doping to obtain higher  $zT$  values. Nevertheless, phosphorus losses at moderate temperatures and potential stability issues under ambient conditions are likely to limit its practical applicability in thermoelectric devices. Similar issues might exist in other phosphorus-rich phosphides.

## CONCLUSION

We deposited amorphous  $\text{CuP}_{2+x}$  thin films with a wide range of  $x$  (positive and negative) by reactive sputtering in a  $\text{PH}_3/\text{Ar}$

**Table 1. List of Electrical, Optical, and Thermal Properties Measured in This Study on Postannealed CuP<sub>2+x</sub> Films at Room Temperature<sup>a</sup>**

electrical conductivity	0.5–1.0	S/cm
Seebeck coefficient	+390 ± 10	μV/K
thermal conductivity	1.1 ± 0.1	W/(K m)
band gap	1.5 ± 0.1	eV
work function	5.0 ± 0.1	eV
dielectric constant ( $\epsilon_{\infty}$ )	10.5 ± 1.0	

<sup>a</sup>The film composition is CuP<sub>2.0</sub> for all properties except for the thermal conductivity (CuP<sub>1.35</sub>).

atmosphere. By annealing these films above their crystallization temperature in an inert atmosphere, we observed that the CuP<sub>2</sub> phase was thermodynamically unstable with respect to the Cu<sub>3</sub>P phase. However, it was possible to kinetically stabilize polycrystalline CuP<sub>2</sub> by satisfying all the following conditions: (1) amorphous precursors mixed on the atomic level (rather than a heterogeneous mixture of amorphous components) to ensure the correct local bonding environment; (2) initial composition sufficiently close to the ideal P/Cu ratio of 2, also to ensure the correct local bonding environment; (3) annealing temperature just high enough to allow for solid-state diffusion; (4) annealing time just long enough for crystallization to be completed, but not long enough for a large fraction of P to diffuse to the surface.

Remarkably, amorphous films that were either too P-poor or too P-rich quickly decomposed into Cu<sub>3</sub>P and gaseous phosphorus upon heating. This “compositional lock-in” behavior highlights the importance of pre-existing short-range order for kinetic stabilization of materials under conditions where decomposition and crystallization are in competition with each other.

Polycrystalline CuP<sub>2+x</sub> films are semiconductors with native p-type conductivity. Their electrical properties are rather insensitive to elemental composition in the vicinity of the stoichiometric point and only moderately affected by the annealing conditions. The thermal conductivity of a P-poor CuP<sub>2</sub> film is 1.1 W/(K m) at room temperature, confirming its potential applicability as a thermoelectric material. However, the hole conductivity of CuP<sub>2</sub> is too low to achieve a high power factor (and therefore a high  $zT$  value) without extrinsic doping. Furthermore, decomposition of CuP<sub>2</sub> into Cu<sub>3</sub>P and gaseous phosphorus at around 400 °C hinders high-temperature applications. Although stability issues are not mentioned in the CuP<sub>2</sub> single-crystal literature, our polycrystalline CuP<sub>2+x</sub> films were only stable in ambient conditions for a few days. It is currently not clear if this issue is related to the porous morphology of our films or if it is an intrinsic behavior of CuP<sub>2</sub>.

Finally, CuP<sub>2</sub> is a stronger light absorber than many established photovoltaic materials, with absorption coefficient rapidly rising to 10<sup>5</sup> cm<sup>-1</sup> above its 1.5 eV band gap. Combined with a native doping density in the optimal range for a photovoltaic absorber in a pn junction solar cell (10<sup>15</sup>–10<sup>17</sup> cm<sup>-3</sup>), we conclude that CuP<sub>2</sub> may deserve more detailed optoelectronic characterization.

## EXPERIMENTAL DETAILS

**Film Growth.** Amorphous CuP<sub>2+x</sub> thin films were deposited on Corning Eagle XG borosilicate glass by reactive radio frequency (RF) sputtering over a 10 × 5 cm<sup>2</sup> area. A Cu target and a Cu<sub>3</sub>P target were cosputtered at 2 Pa total pressure in a 5% PH<sub>3</sub>/Ar atmosphere without intentional heating and without substrate rotation. The

targets were oriented so that one short side of the substrate would mainly be coated by the Cu target and the other short side by the Cu<sub>3</sub>P target.

Immediately after deposition, CuP<sub>2+x</sub> films were cut into smaller pieces and annealed in a lamp-based rapid thermal annealing (RTA) furnace in a N<sub>2</sub> atmosphere. Because of the sputtering target geometry and differences in their applied power, small gradients in P/Cu ratio and film thickness were obtained across the substrate. These gradients enabled us to characterize several data points (“samples”) for each annealing run, each with a distinct composition and thickness. More details on film deposition and annealing are available in the [Supporting Information](#).

**Film Characterization.** All measurements except for nanocalorimetry and thermoelectric/Hall effect characterization were performed within 24 h after annealing to avoid sample degradation. The combinatorial characterization data arising from compositional gradients in the films were managed with the COMBIgor tool<sup>46</sup> and the Research Data Infrastructure<sup>47</sup> and integrated into the High-Throughput Experimental Materials Database.<sup>48</sup>

Elemental composition and film thickness were determined by X-ray fluorescence (XRF) calibrated by Rutherford backscattering spectrometry (RBS, composition) and spectroscopic ellipsometry (thickness). X-ray diffraction (XRD) measurements were conducted by using Cu K $\alpha$  radiation, a 2D detector, and a fixed incidence angle of 10°. Raman spectra were measured with 532 nm excitation wavelength and 4 W/mm<sup>2</sup> power density. Scanning electron microscopy (SEM) images were taken at 5 kV beam voltage.

Sheet resistance was measured with a collinear four-point probe directly contacting the film. The Seebeck coefficient of a CuP<sub>2</sub> film on glass was measured in a custom-built setup by using In contacts. The work function was measured with a Kelvin probe calibrated with a standard Au sample. The absorption coefficient and optical functions were extracted by spectroscopic ellipsometry. Because of higher porosity in the upper part of the film, we modeled the system as a glass substrate of known optical functions, a CuP<sub>2</sub> layer with a linearly increasing fraction of air from bottom to top,<sup>49</sup> and a roughness layer treated with Bruggeman effective medium theory.

For nanocalorimetry and thermoelectric/Hall effect characterization, CuP<sub>2+x</sub> films were deposited on previously described microfabricated chips designed for calorimetry<sup>50</sup> and in-plane thermoelectric characterization<sup>40</sup> of thin-film samples. In both types of chips, CuP<sub>2+x</sub> was deposited on a free-standing Si<sub>3</sub>N<sub>4</sub> membrane. Because of the fragility of the membrane, thinner CuP<sub>2+x</sub> films (90–120 nm) were employed for these studies.

Nanocalorimetry experiments were conducted in a N<sub>2</sub> atmosphere on an as-deposited amorphous film with initial CuP<sub>2.5</sub> composition, with an average heating rate of roughly 5000 °C/s. Temperature-dependent thermoelectric characterization (electrical and thermal conductivity and Seebeck coefficient) was performed in a vacuum on three films with different compositions after annealing. The electrical conductivity was measured by using the van der Pauw (vdP) method.<sup>51</sup> The Seebeck coefficient was measured with respect to platinum metals lines by using an internal four-probe platinum thermometer.<sup>40</sup> The thermal conductivity was derived from the current–voltage characteristics of membrane heaters/thermometers in the self-heating regime.<sup>40,52</sup> The hole concentration and mobility were measured on the same samples by double AC Hall.<sup>53</sup> More details on all measurements are available in the [Supporting Information](#).

## ASSOCIATED CONTENT

### Supporting Information

The Supporting Information is available free of charge at <https://pubs.acs.org/doi/10.1021/jacs.2c04868>.

EDX analysis of a multiphase film, XRD patterns as a function of composition and annealing conditions, electrical conductivity close to the ideal CuP<sub>2</sub> stoichiometry, complex dielectric function spectra, RBS



spectra used for calibration of elemental composition, simulation of Seebeck coefficient of  $\text{CuP}_2$ , additional thermoelectric characterization data (PDF)

## AUTHOR INFORMATION

### Corresponding Authors

**Andrea Crovetto** – Materials Science Center, National Renewable Energy Laboratory, Golden, Colorado 80401, United States; Department of Structure and Dynamics of Energy Materials, Helmholtz-Zentrum Berlin für Materialien und Energie GmbH, 14109 Berlin, Germany; [orcid.org/0000-0003-1499-8740](https://orcid.org/0000-0003-1499-8740); Email: [ancro@dtu.dk](mailto:ancro@dtu.dk)

**Andriy Zakutayev** – Materials Science Center, National Renewable Energy Laboratory, Golden, Colorado 80401, United States; [orcid.org/0000-0002-3054-5525](https://orcid.org/0000-0002-3054-5525); Email: [andriy.zakutayev@nrel.gov](mailto:andriy.zakutayev@nrel.gov)

### Authors

**Danny Kojda** – Department Dynamics and Transport in Quantum Materials, Helmholtz-Zentrum Berlin für Materialien und Energie GmbH, 14109 Berlin, Germany; [orcid.org/0000-0001-6196-4637](https://orcid.org/0000-0001-6196-4637)

**Feng Yi** – Material Measurement Laboratory, National Institute of Standards and Technology, Gaithersburg, Maryland 20899, United States; [orcid.org/0000-0002-8269-3685](https://orcid.org/0000-0002-8269-3685)

**Karen N. Heinselman** – Materials Science Center, National Renewable Energy Laboratory, Golden, Colorado 80401, United States; [orcid.org/0000-0003-0287-3019](https://orcid.org/0000-0003-0287-3019)

**David A. LaVan** – Material Measurement Laboratory, National Institute of Standards and Technology, Gaithersburg, Maryland 20899, United States

**Klaus Habicht** – Department Dynamics and Transport in Quantum Materials, Helmholtz-Zentrum Berlin für Materialien und Energie GmbH, 14109 Berlin, Germany; Institute of Physics and Astronomy, University of Potsdam, 14476 Potsdam, Germany; [orcid.org/0000-0002-9915-7221](https://orcid.org/0000-0002-9915-7221)

**Thomas Unold** – Department of Structure and Dynamics of Energy Materials, Helmholtz-Zentrum Berlin für Materialien und Energie GmbH, 14109 Berlin, Germany; [orcid.org/0000-0002-5750-0693](https://orcid.org/0000-0002-5750-0693)

Complete contact information is available at:

<https://pubs.acs.org/10.1021/jacs.2c04868>

### Notes

The authors declare no competing financial interest.

## ACKNOWLEDGMENTS

This project has received funding from the European Union's Horizon 2020 research and innovation programme under the Marie Skłodowska-Curie Grant Agreement No. 840751 (synthesis work and most characterization and analysis work). This work was authored in part at the National Renewable Energy Laboratory, operated by Alliance for Sustainable Energy, LLC, for the U.S. Department of Energy (DOE) under Contract DE-AC36-08GO28308. Funding supporting development and operation of synthesis and characterization equipment was provided by the Office of Science, Office of Basic Energy Sciences. The authors gratefully acknowledge support of the Helmholtz Energy Materials Foundry (HEMF). Certain commercial equipment, instru-

ments, or materials are identified in this document. Such identification does not imply recommendation or endorsement by the National Institute of Standards and Technology (NIST), nor does it imply that the products identified are necessarily the best available for the purpose. Nanocalorimeter fabrication was performed in part at the NIST Center for Nanoscale Science & Technology (CNST).

## REFERENCES

- (1) Pöttgen, R.; Hönle, W.; von Schnering, H. G. *Encyclopedia of Inorganic and Bioinorganic Chemistry*; John Wiley and Sons, Ltd.: Chichester, UK, 2011.
- (2) Corbridge, D. E. C. *Phosphorus: Chemistry, Biochemistry and Technology*, 6th ed.; CRC Press: 2013; p 608.
- (3) Samuel, V.; Rao, V. J. Optical and valence band studies of  $\text{ZnP}_2$  thin films. *J. Mater. Res.* **1989**, *4*, 185–188.
- (4) Denis, V. A.; Sheleg, A. U.; Unyarkha, L. S. Crystallization kinetics and phase transformations of zinc- and cadmium diphosphide films. *Crystal Research and Technology* **1989**, *24*, 585–590.
- (5) Haraldsen, H. Beiträge zur systematischen Verwandtschaftslehre. 87. Über die Phosphide des Kupfers. *Zeitschrift für anorganische und allgemeine Chemie* **1939**, *240*, 337–354.
- (6) Juza, R.; Bär, K. Leiter und Halbleiter unter den Phosphiden der ersten und zweiten Nebengruppe. *Zeitschrift für anorganische und allgemeine Chemie* **1956**, *283*, 230–245.
- (7) Olofsson, O.; et al. The Crystal Structures of  $\text{CuP}_2$  and  $\text{AgP}_2$  with some Phase Analytical Data of the Cu-P and Ag-P Systems. *Acta Chem. Scand.* **1965**, *19*, 229–241.
- (8) Goryunova, N. A.; Orlov, V. M.; Sokolova, V. I.; Shpenkov, G. P.; Tsvetkova, E. V. Preparation and some properties of  $\text{CuP}_2$  single crystals. *Physica Status Solidi (b)* **1968**, *25*, 513–519.
- (9) Odile, J. P.; Soled, S.; Castro, C. A.; Wold, A. Crystal growth and characterization of the transition-metal phosphides copper diphosphide, nickel diphosphide, and rhodium triphosphide. *Inorg. Chem.* **1978**, *17*, 283–286.
- (10) Kloc, C.; Lux-Steiner, M.; Keil, M.; Baumann, J.; Döll, G.; Bucher, E. Growth and characterization of  $\text{CuP}_2$  single crystals. *J. Cryst. Growth* **1990**, *106*, 635–642.
- (11) von Känel, H.; Gantert, L.; Hauger, R.; Wachter, P. Photoelectrochemical production of hydrogen from p-type transition metal phosphides. *Int. J. Hydrogen Energy* **1985**, *10*, 821–827.
- (12) Pöhls, J.-H.; Faghaninia, A.; Petretto, G.; Aydemir, U.; Ricci, F.; Li, G.; Wood, M.; Ohno, S.; Hautier, G.; Snyder, G. J.; Rignanese, G.-M.; Jain, A.; White, M. A. Metal phosphides as potential thermoelectric materials. *J. Mater. Chem. C* **2017**, *5*, 12441–12456.
- (13) Jong, U.-G.; Ri, C.-H.; Pak, C.-J.; Kim, C.-H.; Cottenier, S.; Yu, C.-J. Metal phosphide  $\text{CuP}_2$  as a promising thermoelectric material: an insight from a first-principles study. *New J. Chem.* **2021**, *45*, 21569–21576.
- (14) Riyajuddin, S.; Azmi, K.; Pahuja, M.; Kumar, S.; Maruyama, T.; Bera, C.; Ghosh, K. Super-Hydrophilic Hierarchical Ni-Foam-Graphene-Carbon Nanotubes- $\text{Ni}_2\text{P}$ - $\text{CuP}_2$  Nano-Architecture as Efficient Electrocatalyst for Overall Water Splitting. *ACS Nano* **2021**, *15*, 5586–5599.
- (15) Kim, S.-O.; Manthiram, A. Phosphorus-Rich  $\text{CuP}_2$  Embedded in Carbon Matrix as a High-Performance Anode for Lithium-Ion Batteries. *ACS Appl. Mater. Interfaces* **2017**, *9*, 16221–16227.
- (16) Harper, A. F.; Evans, M. L.; Morris, A. J. Computational Investigation of Copper Phosphides as Conversion Anodes for Lithium-Ion Batteries. *Chem. Mater.* **2020**, *32*, 6629–6639.
- (17) Liu, Z.; Yang, S.; Sun, B.; Yang, P.; Zheng, J.; Li, X. Low-Temperature Synthesis of Honeycomb  $\text{CuP}_2$ @C in Molten  $\text{ZnCl}_2$  Salt for High-Performance Lithium Ion Batteries. *Angew. Chem., Int. Ed.* **2020**, *59*, 1975–1979.
- (18) Chen, S.; Wu, F.; Shen, L.; Huang, Y.; Sinha, S. K.; Srot, V.; van Aken, P. A.; Maier, J.; Yu, Y. Cross-Linking Hollow Carbon Sheet Encapsulated  $\text{CuP}_2$  Nanocomposites for High Energy Density Sodium-Ion Batteries. *ACS Nano* **2018**, *12*, 7018–7027.

- (19) Zhang, Y.; Wang, G.; Wang, L.; Tang, L.; Zhu, M.; Wu, C.; Dou, S.-X.; Wu, M. Graphene-Encapsulated CuP<sub>2</sub>: A Promising Anode Material with High Reversible Capacity and Superior Rate-Performance for Sodium-Ion Batteries. *Nano Lett.* **2019**, *19*, 2575–2582.
- (20) Schnepf, R. R.; Crovetto, A.; Gorai, P.; Park, A.; Holtz, M.; Heinselman, K. N.; Bauers, S. R.; Brooks Tellekamp, M.; Zakutayev, A.; Greenaway, A. L.; Toberer, E. S.; Tamboli, A. C. Reactive phosphine combinatorial co-sputtering of cation disordered ZnGeP<sub>2</sub> films. *J. Mater. Chem. C* **2022**, *10*, 870–879.
- (21) Crovetto, A.; Adamczyk, J. M.; Schnepf, R. R.; Perkins, C. L.; Hempel, H.; Bauers, S. R.; Toberer, E. S.; Tamboli, A. C.; Unold, T.; Zakutayev, A. Boron Phosphide Films by Reactive Sputtering: Searching for a P-Type Transparent Conductor. *Advanced Materials Interfaces* **2022**, *9*, 2200031.
- (22) Willis, J.; Bravić, I.; Schnepf, R. R.; Heinselman, K. N.; Monserrat, B.; Unold, T.; Zakutayev, A.; Scanlon, D. O.; Crovetto, A. Prediction and realisation of high mobility and degenerate p-type conductivity in CaCuP thin films. *Chemical Science* **2022**, *13*, 5872.
- (23) Momma, K.; Izumi, F. VESTA 3 for three-dimensional visualization of crystal, volumetric and morphology data. *J. Appl. Crystallogr.* **2011**, *44*, 1272–1276.
- (24) Pearson, W. B. The crystal structures of semiconductors and a general valence rule. *Acta Crystallogr.* **1964**, *17*, 1–15.
- (25) Pauling, L.; Kamb, B. A revised set of values of single-bond radii derived from the observed interatomic distances in metals by correction for bond number and resonance energy. *Proc. Natl. Acad. Sci. U. S. A.* **1986**, *83*, 3569–3571.
- (26) Qi, J.; et al. Dimer rattling mode induced low thermal conductivity in an excellent acoustic conductor. *Nat. Commun.* **2020**, *11*, 5197.
- (27) Jain, A.; Ong, S. P.; Hautier, G.; Chen, W.; Richards, W. D.; Dacek, S.; Cholia, S.; Gunter, D.; Skinner, D.; Ceder, G.; Persson, K. A. Commentary: The Materials Project: A materials genome approach to accelerating materials innovation. *APL Materials* **2013**, *1*, 011002.
- (28) Rachkov, A. G.; Schimpf, A. M. Colloidal Synthesis of Tunable Copper Phosphide Nanocrystals. *Chem. Mater.* **2021**, *33*, 1394–1406.
- (29) Bock, H.; Mueller, H. Gas-phase reactions. 44. The phosphorus P<sub>4</sub> ⇌ 2P<sub>2</sub> equilibrium visualized. *Inorg. Chem.* **1984**, *23*, 4365–4368.
- (30) Aykol, M.; Dwaraknath, S. S.; Sun, W.; Persson, K. A. Thermodynamic limit for synthesis of metastable inorganic materials. *Sci. Adv.* **2018**, *4*, No. eaaq0148.
- (31) Crovetto, A.; Ottsen, T. S.; Stamate, E.; Kjær, D.; Schou, J.; Hansen, O. On performance limitations and property correlations of Al-doped ZnO deposited by radio-frequency sputtering. *J. Phys. D: Appl. Phys.* **2016**, *49*, 295101.
- (32) Wolff, A.; Pallmann, J.; Boucher, R.; Weiz, A.; Brunner, E.; Doert, T.; Ruck, M. Resource-Efficient High-Yield Ionothermal Synthesis of Microcrystalline Cu<sub>3-x</sub>P. *Inorg. Chem.* **2016**, *55*, 8844–8851.
- (33) Ong, S. P.; Cholia, S.; Jain, A.; Brafman, M.; Gunter, D.; Ceder, G.; Persson, K. A. The Materials Application Programming Interface (API): A simple, flexible and efficient API for materials data based on REpresentational State Transfer (REST) principles. *Comput. Mater. Sci.* **2015**, *97*, 209–215.
- (34) Petretto, G.; Dwaraknath, S.; Miranda, H. P. C.; Winston, D.; Giantomassi, M.; van Setten, M. J.; Gonze, X.; Persson, K. A.; Hautier, G.; Rignanese, G.-M. High-throughput density-functional perturbation theory phonons for inorganic materials. *Sci. Data* **2018**, *5*, 180065.
- (35) Kroumova, E.; Aroyo, M.; Perez-Mato, J.; Kirov, A.; Capillas, C.; Ivantchev, S.; Wondratschek, H. Bilbao Crystallographic Server: Useful Databases and Tools for Phase-Transition Studies. *Phase Transitions* **2003**, *76*, 155–170.
- (36) Nishigaki, Y.; Nagai, T.; Nishiwaki, M.; Aizawa, T.; Kozawa, M.; Hanzawa, K.; Kato, Y.; Sai, H.; Hiramatsu, H.; Hosono, H.; Fujiwara, H. Extraordinary Strong Band-Edge Absorption in Distorted Chalcogenide Perovskites. *Solar RRL* **2020**, *4*, 1900555.
- (37) Crovetto, A.; Hajjifarassar, A.; Hansen, O.; Seger, B.; Chorkendorff, I.; Vesborg, P. C. K. Parallel Evaluation of the BiI<sub>3</sub>, BiOI, and Ag<sub>3</sub>BiI<sub>6</sub> Layered Photoabsorbers. *Chem. Mater.* **2020**, *32*, 3385–3395.
- (38) Crovetto, A.; Xing, Z.; Fischer, M.; Nielsen, R.; Savory, C. N.; Rindzevicius, T.; Stenger, N.; Scanlon, D. O.; Chorkendorff, I.; Vesborg, P. C. K. Experimental and First-Principles Spectroscopy of Cu<sub>2</sub>SrSnS<sub>4</sub> and Cu<sub>2</sub>BaSnS<sub>4</sub> Photoabsorbers. *ACS Appl. Mater. Interfaces* **2020**, *12*, 50446–50454.
- (39) Yu, P. Y.; Cardona, M. *Fundamentals of Semiconductors*; Graduate Texts in Physics; Springer: Berlin, 2010.
- (40) Linseis, V.; Völklein, F.; Reith, H.; Nielsch, K.; Woias, P. Advanced platform for the in-plane ZT measurement of thin films. *Rev. Sci. Instrum.* **2018**, *89*, 015110.
- (41) May, A. F.; Snyder, G. J. In *Thermoelectrics and Its Energy Harvesting*; Rowe, D. M., Ed.; CRC Press: 2012; Chapter 11.
- (42) Madsen, G. K.; Carrete, J.; Verstraete, M. J. BoltzTraP2, a program for interpolating band structures and calculating semi-classical transport coefficients. *Comput. Phys. Commun.* **2018**, *231*, 140–145.
- (43) Cahill, D. G.; Pohl, R. O. Lattice Vibrations and Heat Transport in Crystals and Glasses. *Annu. Rev. Phys. Chem.* **1988**, *39*, 93–121.
- (44) Liu, W.; Asheghi, M. Thermal Conductivity Measurements of Ultra-Thin Single Crystal Silicon Layers. *Journal of Heat Transfer* **2006**, *128*, 75–83.
- (45) Kojda, D.; Hofmann, T.; Gostkowska-Lekner, N.; Habicht, K. Characterization and modeling of the temperature-dependent thermal conductivity in sintered porous silicon-aluminum nanomaterials. *Nano Research* **2022**, 1–8.
- (46) Talley, K. R.; Bauers, S. R.; Melamed, C. L.; Papac, M. C.; Heinselman, K. N.; Khan, I.; Roberts, D. M.; Jacobson, V.; Mis, A.; Brennecke, G. L.; Perkins, J. D.; Zakutayev, A. COMBIgor: Data-Analysis Package for Combinatorial Materials Science. *ACS Comb. Sci.* **2019**, *21*, 537–547.
- (47) Talley, K. R.; White, R.; Wunder, N.; Eash, M.; Schwarting, M.; Evenson, D.; Perkins, J. D.; Tumas, W.; Munch, K.; Phillips, C.; Zakutayev, A. Research data infrastructure for high-throughput experimental materials science. *Patterns* **2021**, *2*, 100373.
- (48) Zakutayev, A.; Wunder, N.; Schwarting, M.; Perkins, J. D.; White, R.; Munch, K.; Tumas, W.; Phillips, C. An open experimental database for exploring inorganic materials. *Sci. Data* **2018**, *5*, 180053.
- (49) Crovetto, A.; Cazzaniga, A.; Ettliger, R. B.; Schou, J.; Hansen, O. Large process-dependent variations in band alignment and interface band gaps of Cu<sub>2</sub>ZnSnS<sub>4</sub>/CdS solar cells. *Sol. Energy Mater. Sol. Cells* **2018**, *187*, 233–240.
- (50) Yi, F.; LaVan, D. A. Nanocalorimetry: Exploring materials faster and smaller. *Applied Physics Reviews* **2019**, *6*, 031302.
- (51) van der Pauw, L. J. A method of measuring specific resistivity and Hall effect of discs of arbitrary shape. *Philips Research Reports* **1958**, *13*, 1–9.
- (52) Völklein, F.; Reith, H.; Meier, A. Measuring methods for the investigation of in-plane and cross-plane thermal conductivity of thin films. *Physica Status Solidi (a)* **2013**, *210*, 106–118.
- (53) Kasai, A.; Abdulla, A.; Watanabe, T.; Takenaga, M. Highly Sensitive Precise Double AC Hall Effect Apparatus for Wide Resistance Range. *Jpn. J. Appl. Phys.* **1994**, *33*, 4137–4145.